Supporting Information for

Ordered Mesoporous Electrocatalysts for Highly Selective Formate Production from Electrocatalytic CO_2 Reduction

Ashfaq Ahamd,[1,#] Chaoran Zhang,[1,#] Yichuan Gu, Qu Jiang,[1] Ziyang Sheng,[1] Ruohan Feng,[1] Sihong Wang,[1] Haoyue Zhang,[1] Qianqing Xu,[1] Zijian Yuan,[1] Fang Song [1,*]

[1]State Key Laboratory of Metal Matrix Composites, School of Materials Science and Engineering, Shanghai Jiao Tong University, Shanghai 200240, China

[#]Ashfaq Ahamd and Chaoran Zhang contributed equally to this paper.

[*] Corresponding authors: songfang@sjtu.edu.cn

Supplementary Figures

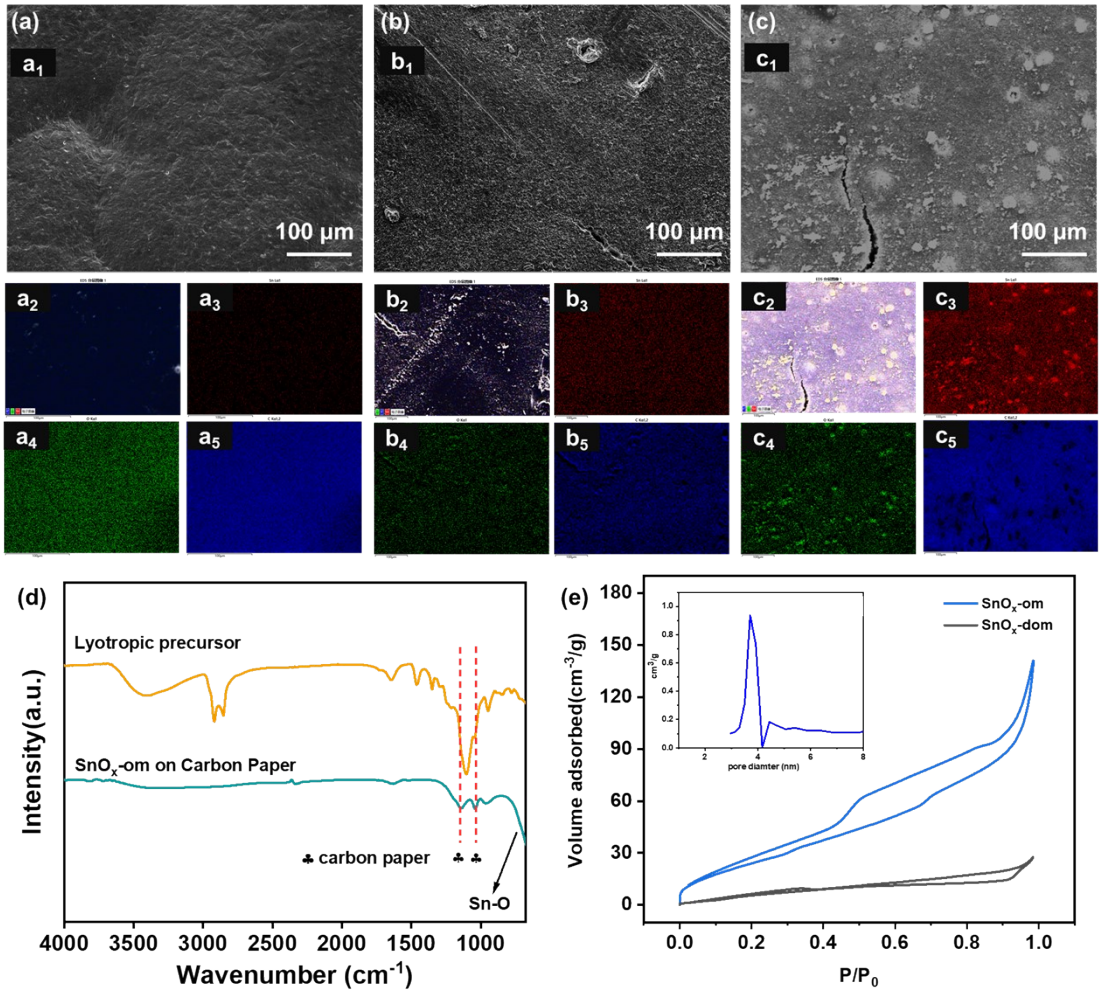

Figure S1. a, b, c) SEM images and elemental distributions of a) Brij 56 on carbon paper, b) lyotropic precursor on carbon paper, and c) as-deposited SnO_x-om on carbon paper. c_2, d_2 and e_2 are overlapped elemental distribution of Brij 56, lyotropic precursor and as-deposited SnO_x-om. a_3, b_3 and c_3 are Sn; a_4, b_4 and c_4 are O; a_5, b_5 and c_5 are C. a) Fourier-transformed infrared spectroscopy of lyotropic precursor (orange line) and SnO_x-om after template removal (green line); b) Nitrogen adsorption-desorption isotherm of SnO_x-om and SnO_x-dom. Inset in b) shows the pore size distribution.

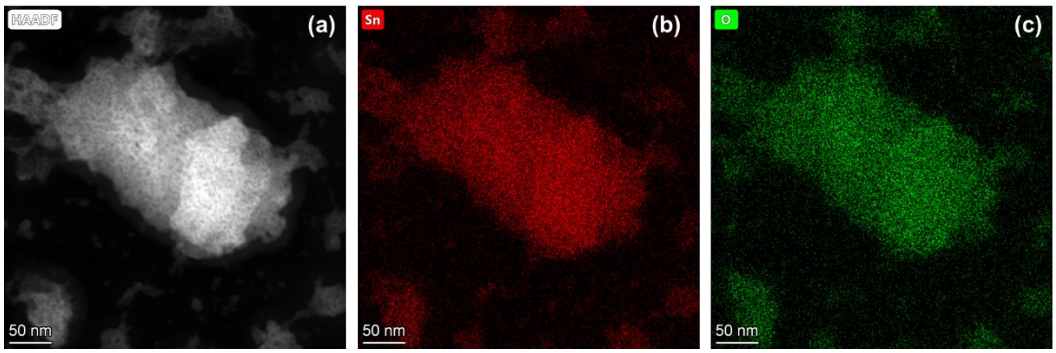

Figure S2. Elemental mapping of SnO_x-om. a) HAADF image, b) Sn, and c) O distribution of SnO_x-om. The spatial distributions of Sn and O in b, c) are depicted in red and green, respectively

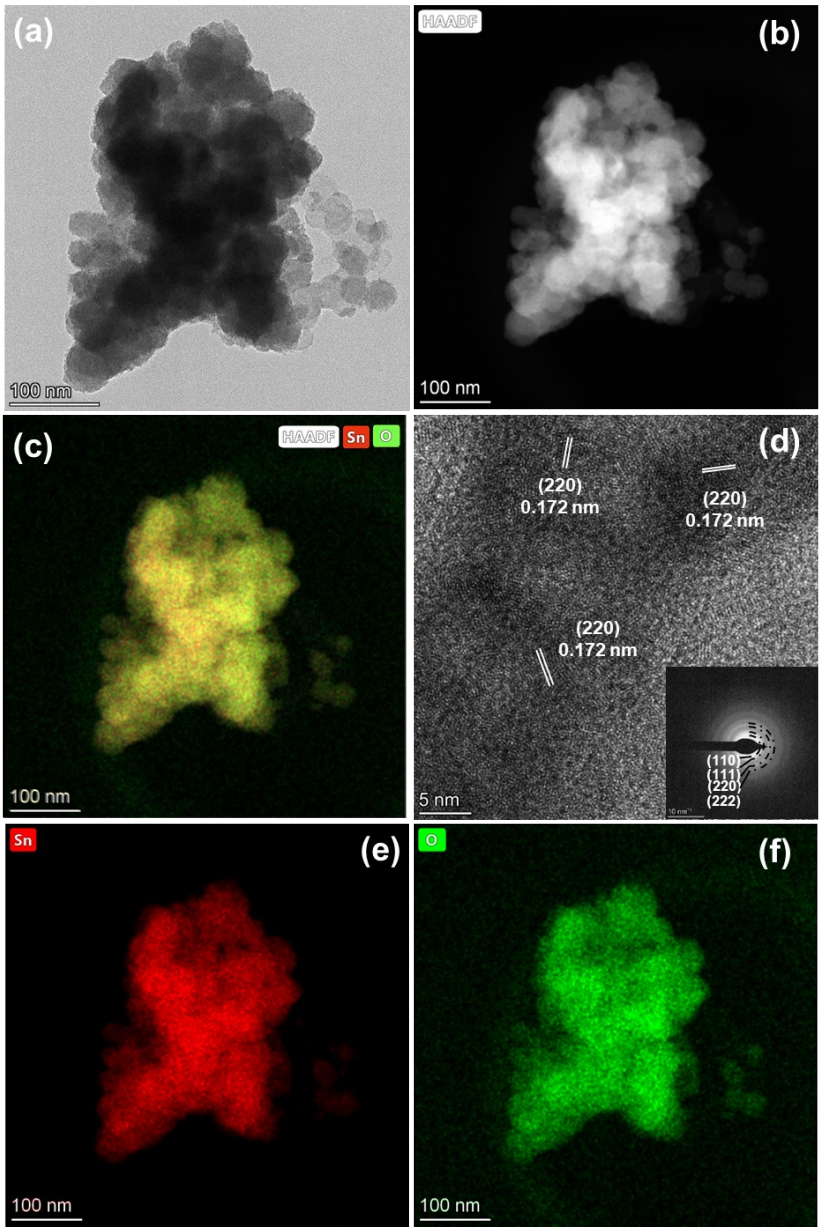

Figure S3. Microstructures of SnO_x-dom. a) TEM image, b) HAADF image, c) EDS mapping, d) HRTEM image, e) Sn and f) O distribution of SnO_x-dom. The inset in d) is the SAED pattern of the corresponding area. The spatial distributions of Sn and O in c, e, f) are depicted in red and green, respectively. The yellow coloration arises from the blending of these colors, indicating a homogeneous distribution of tin and oxygen.

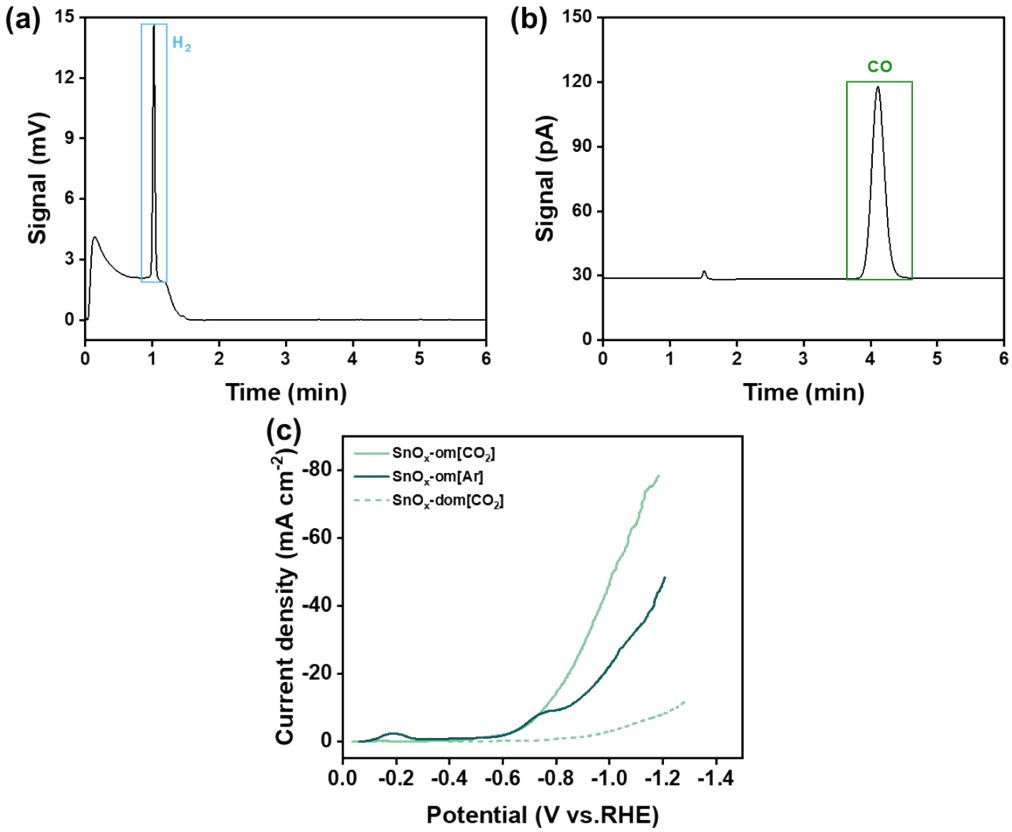

Figure S4. Gas chromatography data and electrochemical analysis for CO_2RR. a) TCD singal curve for H_2; b) FID singla curve for CO; c) LSV curves of SnO_x-om under CO_2-saturated and Ar-saturated 0.1 M $KHCO_3$ and SnO_x-dom under CO_2-saturated 0.1 M $KHCO_3$.

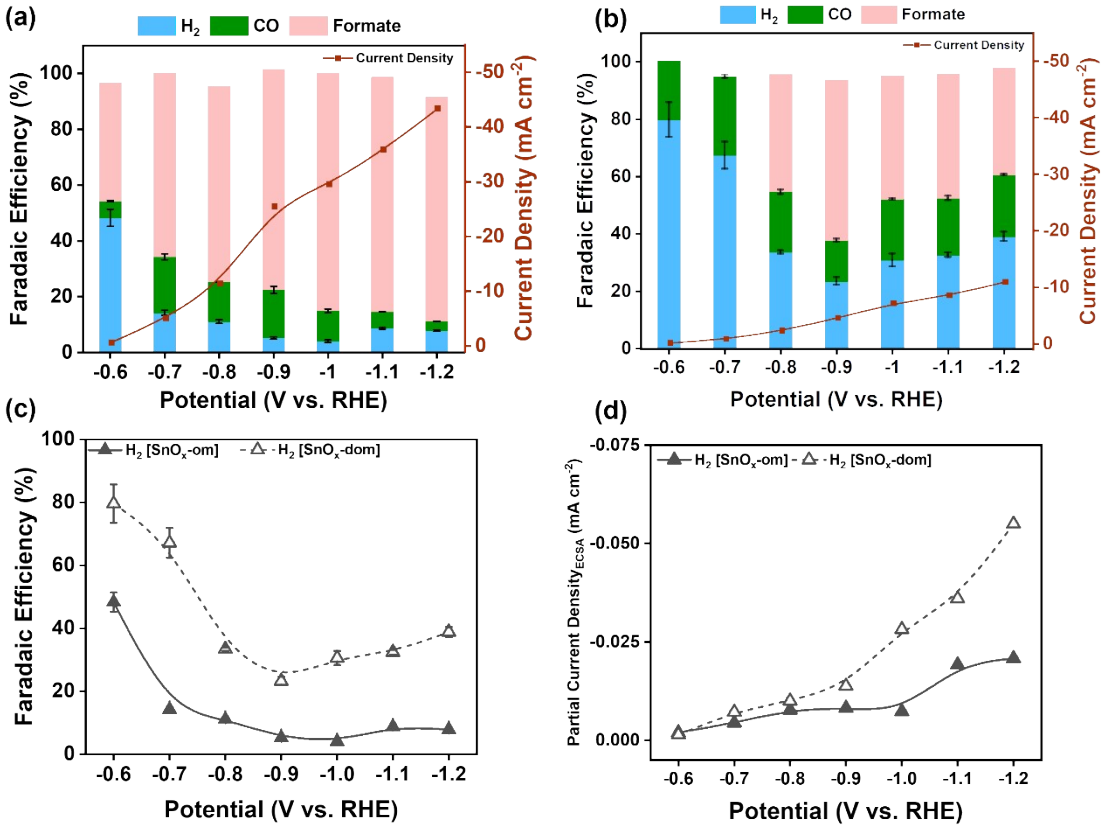

Figure S5. Total current density and Faradaic efficiency of the main CO_2RR products of a) SnO_x-om and b) SnO_x-dom; c) Faradaic efficiency of H_2 plotting against applied potentials; ECSA-normalized H_2 partial current densities plotting against applied potentials.

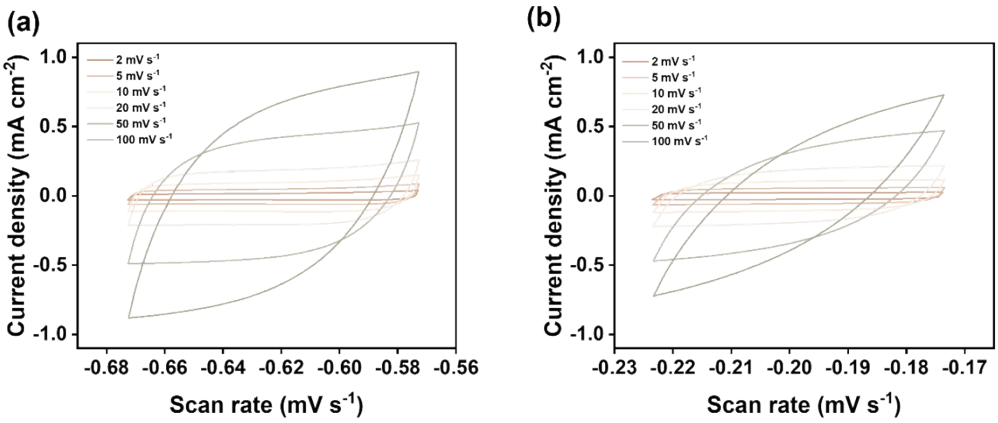

Figure S6. Double-layer cyclic voltammograms at scan rates ranging from 2 to 100 mV s^{-1}**.** a) SnO_x-om and b) SnO_x-dom.

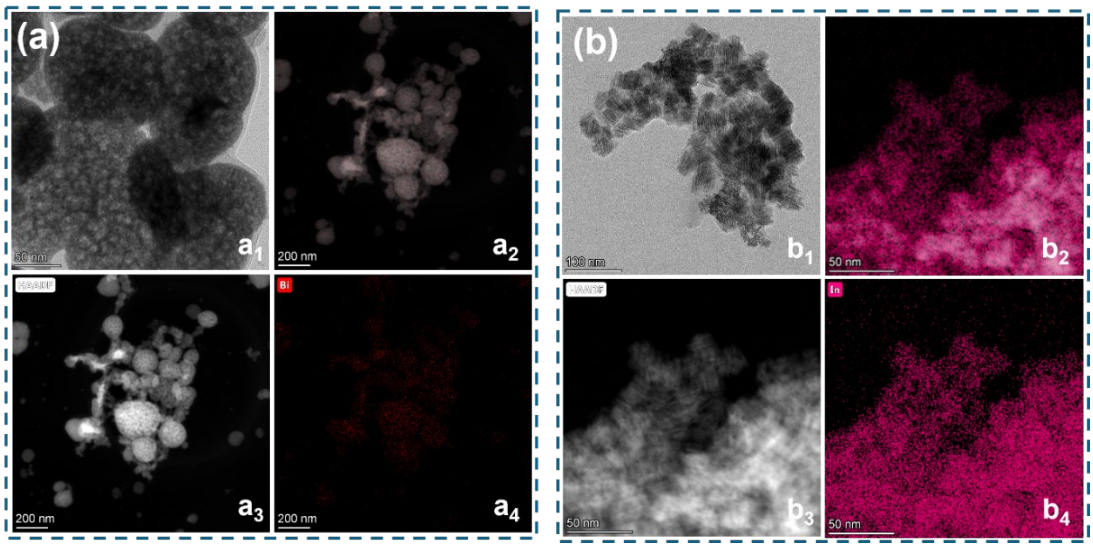

Figure S7. Microstructures of a) BiO_x-om and b) InO_x-om. a_1) TEM image, a_2) overlapped images of a_3) and a_4), a_3) HAADF image and a_4) elemental distribution of Bi of BiO_x-om; b_1) TEM image, b_2) overlapped images of b_3) and b_4), b_3) HAADF image and b_4) elemental distribution of In of InO_x-om.

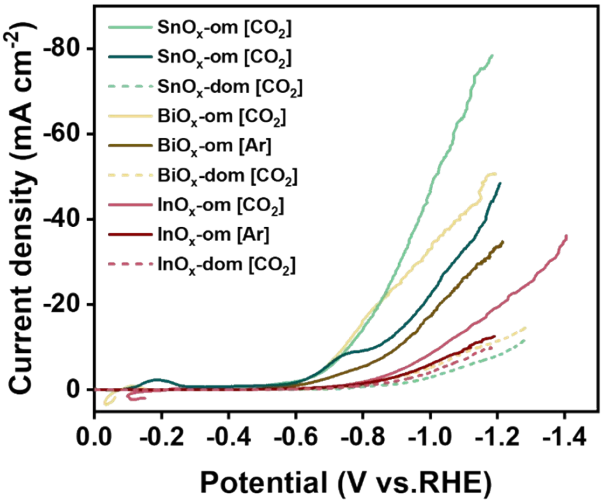

Figure S8. LSV curves of SnO_x-om, BiO_x-om, and InO_x-om under Ar and CO_2-saturated 0.1 M $KHCO_3$ and SnO_x-dom, BiO_x-dom, and InO_x-dom under CO_2-saturated 0.1 M $KHCO_3$.

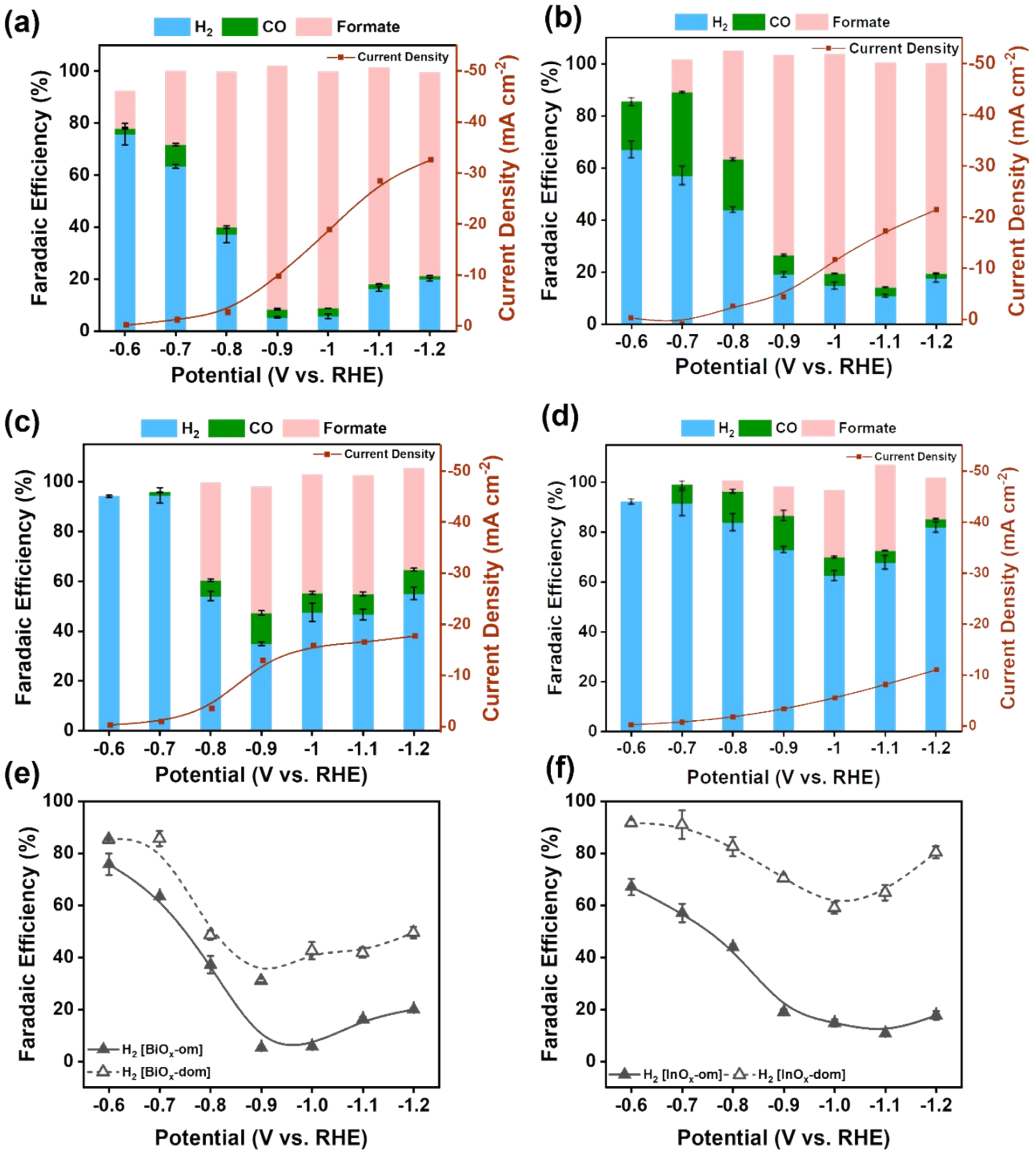

Figure S9. Total current density and Faradaic efficiency of the main CO_2RR products of a) BiO_x-om, b) BiO_x-dom, c) InO_x-om and d) InO_x-dom; e) Faradaic efficiency of H_2 for BiO_x-om and BiO_x-dom plotting against applied potentials; f) Faradaic efficiency of H_2 for InO_x-om and InO_x-dom plotting against applied potentials.

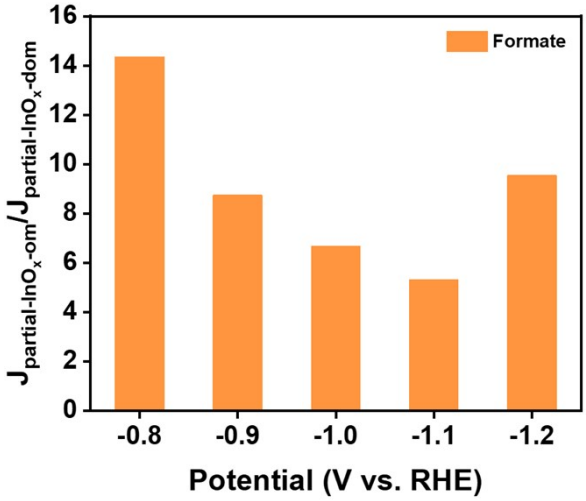

Figure S10. The partial current density ratio of ordered and disordered mesoporous catalysts plotting against applied potentials for InO_x.

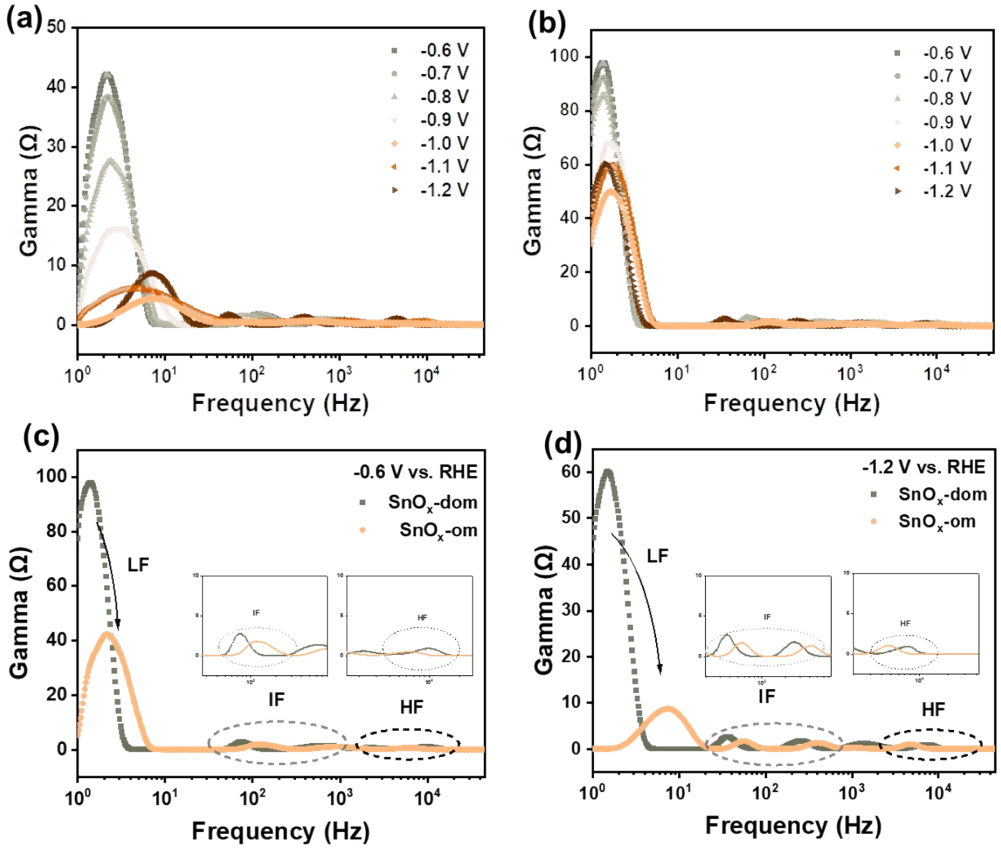

Figure S11. a, b) DRT results at potentials ranging from -0.6V to -1.2 V vs. RHE for a) SnO_x-om and b) SnO_x-dom; c, d) DRT results for electrochemical impedance at a) -0.6 V vs. RHE and b) -1.2 V vs. RHE; Inset in c) and d) is the enlarged view of IF and HF region.

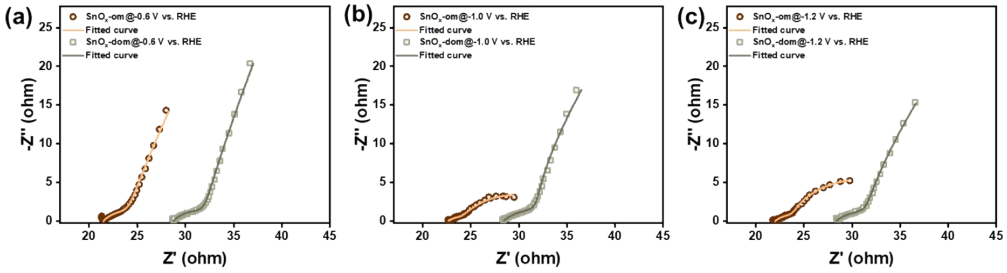

Figure S12. Electrochemical impedance spectra analysis. Nyquist plots and fitting results for electrochemical impedance at a) -0.6 V vs. RHE, b) -1.0 V vs. RHE, and c) -1.2 V vs. RHE.

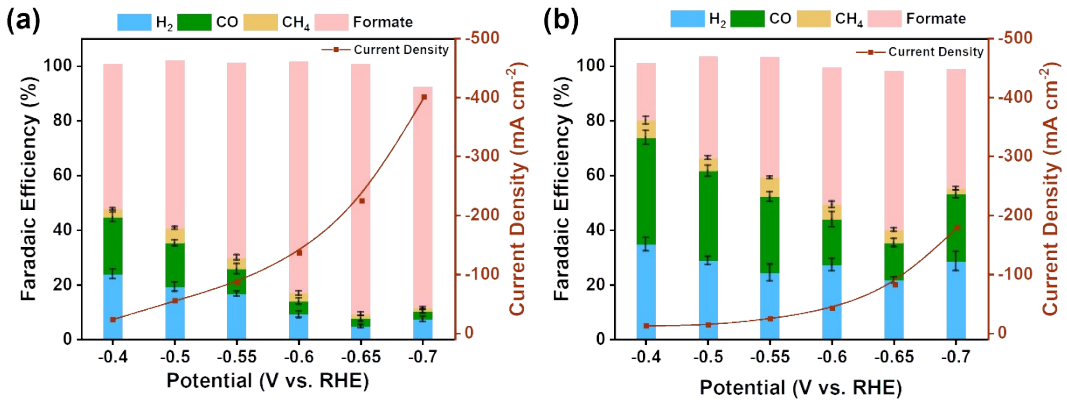

Figure S13. Total current density and Faradaic efficiency of the main CO_2RR products in a flow cell for a) SnO_x-om, b) SnO_x-dom.

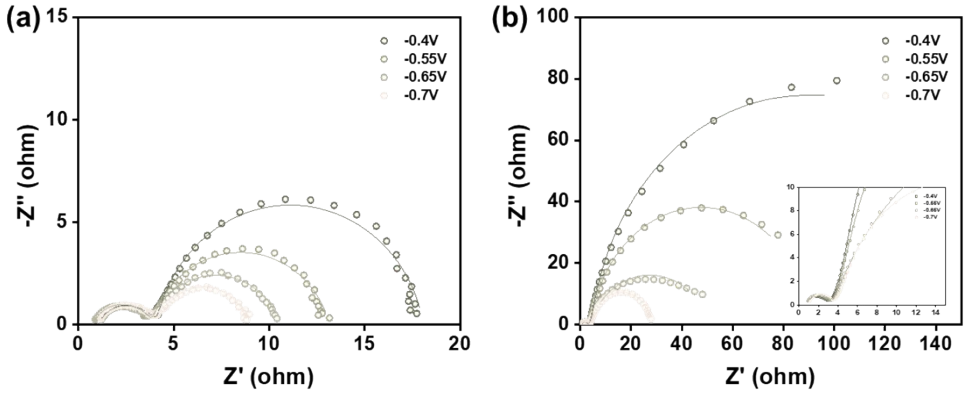

Figure S14. Electrochemical impedance spectra analysis. a, b) Nyquist plots of a) SnO_x-om and b) SnO_x-dom. Inset in b) shows the high-frequency region.

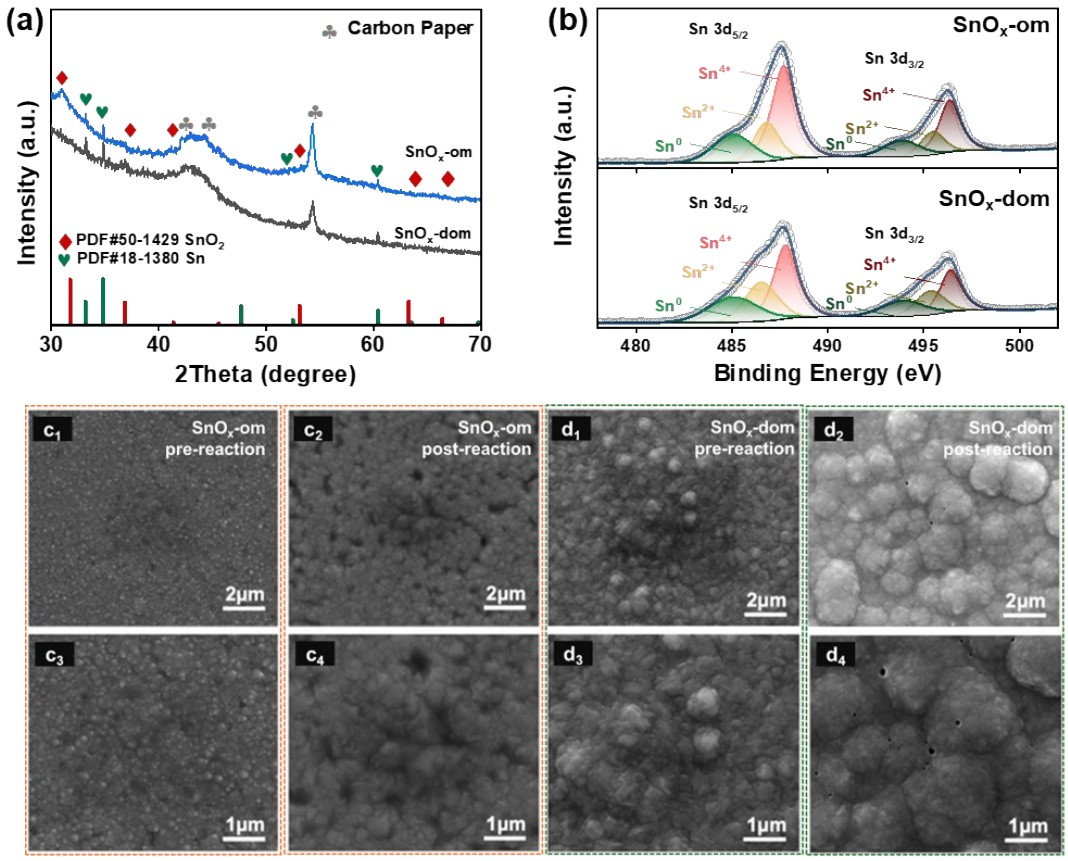

Figure S15. Microstructures of mesoporous catalysts after stability test. a) XRD patterns after the stability test; b) XPS after the stability test; c, d) SEM images before and after stability tests for c) SnO_x-om and d) SnO_x-dom.

Table S1. The gas chromatography data of SnO_x-om.

Potential	H_2 (ppm)			CO (ppm)		
(vs. RHE)	1	2	3	1	2	3
-0.6	410.4986	423.2332	374.2128	51.51025	49.88418	47.11745
-0.7	870.654	980.2331	907.7123	1322.022	1225.406	1360.195
-0.8	1703.888	1579.973	1513.8	2015.761	2060.379	2045.853
-0.9	1728.534	1817.045	1557.446	5305.485	6021.106	5350.31
-1.0	1328.856	1646.866	1582.73	3852.103	4356.4	4032.958
-1.1	3933.039	3879.763	4145.394	2655.824	2638.934	2600.314
-1.2	4391.534	4423.283	4144.134	1789.989	1889.228	1827.147

Table S2. The gas chromatography data of SnO_x-dom

Potential	H_2 (ppm)			CO (ppm)		
(vs. RHE)	1	2	3	1	2	3
-0.6	132.0913	147.1723	-	35.95701	-	-
-0.7	651.7613	728.7713	745.1648	294.8343	287.7133	284.5758
-0.8	975.2981	1008.393	981.4367	593.5576	625.9393	637.6621
-0.9	1448.791	1331.761	1300.989	794.8067	835.77	854.4894
-1.0	2991.337	2585.978	2760.33	1929.972	1898.357	1943.584
-1.1	3472.943	3641.785	3526.372	2074.252	2241.889	2137.805
-1.2	5282.894	5305.547	5673.569	3022.337	2964.336	3006.949

Table S3. The gas chromatography data of BiO_x-om

Potential	H_2 (ppm)			CO (ppm)		
(vs. RHE)	1	2	3	1	2	3
-0.6	162.0153	145.2543	154.4082	4.104882	4.406887	5.374828
-0.7	1002.614	990.2161	980.0763	138.8366	129.4233	123.3744
-0.8	1133.579	1321.47	1331.672	75.64551	98.49735	108.8134
-0.9	611.7689	678.5079	669.9295	347.6604	421.4752	393.5863
-1.0	1356.677	1196.667	1585.798	742.0344	728.9373	734.3881
-1.1	5713.131	6219.818	5600.238	616.1124	688.5852	643.4021
-1.2	8085.426	8147.505	8529.902	557.5079	562.6295	564.5626

Table S4. The gas chromatography data of BiO_x-dom

Potential	H_2 (ppm)			CO (ppm)		
(vs. RHE)	1	2	3	1	2	3
-0.6	356.7413	354.2705	356.8179	-	-	-
-0.7	1075.376	1133.908	1066.697	11.93789	-	14.84596
-0.8	2382.19	2529.145	2385.458	260.4907	294.6776	295.1456
-0.9	5818.903	5578.515	5751.343	1878.21	2064.003	2145.855
-1.0	8683.678	9901.687	9994.554	1414.243	1616.967	1650.811
-1.1	9308.513	10205.25	9737.453	1536.814	1791.322	1839.224
-1.2	11772.35	12804.73	12552.29	2027.655	2245.832	2208.754

Table S5. The gas chromatography data of InO_x-om

Potential	H_2 (ppm)			CO (ppm)		
(vs. RHE)	1	2	3	1	2	3
-0.6	227.4846	249.5156	244.6479	71.71309	62.03641	63.26746
-0.7	669.0545	591.8012	621.2782	347.869	350.3255	355.1954
-0.8	1412.272	1438.197	1484.665	617.8836	635.5866	652.8171
-0.9	1125.982	1022.61	1027.529	393.9492	409.4281	432.2904
-1.0	2407.886	2011.326	2156.89	694.7046	683.5001	689.5737
-1.1	2309.053	2502.21	2298.238	678.8895	762.939	716.3304
-1.2	5144.248	4993.594	4314.492	520.3139	512.2307	437.4516

Table S6. The gas chromatography data of InO_x-dom

Potential	H_2 (ppm)			CO (ppm)		
(vs. RHE)	1	2	3	1	2	3
-0.6	300.1111	306.6819	303.9406	-	-	-
-0.7	912.1569	829.8843	832.0333	54.44146	74.63163	79.10253
-0.8	1784.603	1931.889	1835.664	266.5382	293.0515	262.5404
-0.9	3077.685	3026.577	3128.388	624.0646	470.2793	622.9273
-1.0	4196.402	4458.766	4404.096	493.6665	513.0634	541.7127
-1.1	6843.008	7330.356	6846.629	484.185	476.3759	480.6089
-1.2	11291.5	11832.03	11336.4	435.1092	488.9776	459.1055

Table S7. Typical fitting results of Nyqiust plots of SnO_x-om and SnO_x-dom in H-cell.

	R_Ω	C_{dl}	R_p	C_Φ	R_s
SnO_x-om@-0.6V	21.48	6.704E-3	4.299	6.700eE-3	43.92E6
SnO_x-dom@-0.6V	28.76	4.222E-3	4.497	6.460E-3	19.88E6
SnO_x-om@-1.0V	22.60	18.90E-3	2.881	9.550E-3	11.70
SnO_x-dom@-1.0V	28.36	10.07E-3	6.051	4.632E-3	45.05E6
SnO_x-om@-1.2V	21.97	16.17E-3	3.610	6.059E-3	16.00
SnO_x-dom@-1.2V	28.33	10.42E-3	5.276	6.095E-3	14.88E6

Table S8. Typical fitting results of Nyqiust plots of SnO_x-om and SnO_x-dom in flow cell.

	R_Ω	C_{dl}	R_p	C_Φ	R_s
SnO_x-om@-0.65V	6.510	10.85E-6	23.11	8.826E-3	13.05
SnO_x-dom@-0.65V	7.270	18.83e-6	30.89	79.66	150.7

Table S9. Comparisons of the catalytical performance towards formate using Sn-based materials.

Catalyst	$FE_{formate}$ (%)	$J_{formate}$ (mA cm^{-2})	Applied potential (V vs. RHE)	Stability (h)	Cell type	Electrolyte	Ref.
$SnO/Cu_xO/CF$	70	-1152	-1.2	21	Flow cell	1 M KOH	1
$Cu\text{-}SnO_2$	81	-405	-	0.8	Flow cell	1 M KOH	2
	80	-160	-	5			
$SnO_2\text{-}1$	80	-160	-0.9	6	Flow cell	1 M KOH	3
Stanene	93	-7	-0.93	60	H cell	0.1 M $KHCO_3$	4
$Sn–SnS_x$	93.3	-18.6	-1.2	36	H cell	0.1 M $KHCO_3$	5
$R\text{-}CuSnO_3$	93.4	-23.9	-0.9	-	H cell	0.5 M $KHCO_3$	6
	90	~-90	-	90	Flow cell	1 M KOH	
PPIL[4] $-Sn_5Ag_5$	91	~-90	-0.75 to -1.0	30	Flow cell	1 M KOH	7
$Sn_3O(OH)_2Cl_2$	90	-29	-0.9	35	H cell	0.5 M $KHCO_3$	8
	~90	-165	-0.9	40	Flow cell	1 M KOH	
$Sn(SnO_2)_{15}\text{-}CN_x$	82.5	-16.7	-0.78	2	H cell	0.5 M $KHCO_3$	9
$5\%Cu\text{-}SnO_2$	91	-22	-0.9	12	H cell	0.5 M $KHCO_3$	10
	92	~-110.4	-0.9	14	Flow cell	1 M KOH	
$SnS_2@SnO_2$	92.2	~-184.4	-0.86	20	Flow cell	1 M KOH	11
$Cu@Cu\text{-}SnS_2$	93	-35	-1.0	10	H cell	0.5 M $KHCO_3$	12
Dual-phase Cu	93	~-50	-1.4	10	H cell	0.5 M $KHCO_3$	13
$SnO_2/Cu_6Sn_5/CuO$	90.13	-25.2	-0.95	45	H cell	0.5 M $NaHCO_3$	14
	95.64	-70	-0.95	25	Flow cell	1 M KOH	
SnO_x-om	85	-25.11	-1.0	-	H cell	0.1 M $KHCO_3$	**Our work**
	91	-205.5	-0.65	22	Flow cell	1 M KOH	

Supplementary Note 1

The Pourbaix diagram in Figure 5b depicts the dependence of the proton available on the thermodynamics of the CO_2 electroreduction process for the production of formate/formic acid, CH_4, and CH_3OH. It is visualized by plotting the standard potential of the reactant–product couple to the pH, which is calculated according to the Nernst equation [15–17]. For reactions involving proton-coupled electron transfer, E~pH lines are parallel and have a slope of 59.2 mV pH^{-1}. Differently, the E~pH line for CO_2RR to formic acid (or formate) consists of two segments, one with a slope of 59.2 mV pH^{-1} for the production of formic acid at pH < 3.75 (Reaction 1) and the other with a slope of 29.6 mV pH^{-1} for the production of formate at pH > 3.75 (Reaction 2 and 3).

Reation 1: $CO_2 + 2H^+ + 2e^- \rightarrow HCOOH$

Reation 2: $CO_2 + H^+ + 2e^- \rightarrow \quad HCOO^-$

Reation 3: $CO_2 + H_2O + 2e^- \rightarrow HCOO^- + OH^-$

Although the generation of formic acid in an acidic environment is thermodynamically unfavorably, the deprotonation at high pH significantly improves the feasibility of the reaction.

Supplementary Note 2

Before we tested products, we bubbled standard gas with a known concentration of components to calibrate the peak area and get the peak area for certain products, namely S_0-H_2 or S_0-CO. According to Lange's Handbook of Chemistry, the solubility of typical products during the CO_2RR is 3.8 mM for H_2, 0.5 mM for CO, and the solubility of CO_2 is 33 mM. According to the peak integration of tested ones (one example is shown in Figure S4a and S4b), we gained a value of peak area for the generated certain products, namely S_i-H_2 or S_i-CO. Then we are able to use the ratio of S_i-H_2 to S_0-H_2 to know the detailed concentration of target products, namely x_i. For every single data point, we calculated the average value of three sampling points to ensure the accuracy of statistics. The corresponding analysis method refers to several related literatures [18–20].

References

1 T. Liu, K. Ohashi, K. Nagita, T. Harada, S. Nakanishi and K. Kamiya, *Small*, 2022, **18**, 2205323.

2 Y. Jiang, J. Shan, P. Wang, L. Huang, Y. Zheng and S.-Z. Qiao, *ACS Catal.*, 2023, **13**, 3101–3108.

3 Z. Liu, J. Chen, H. Guo and X. Huang, *Nano Energy*, 2023, **108**, 108193.

4 X. Mei, C. Liu, D. Zhang, J. Cao, R. Ge, J. Wang and W. Xu, *Advanced Energy Materials*, 2024, **14**, 2303889.

5 C. Chen, S. Shen, J. Wang, Y. Liu, X. Guo, L. Zhang and J. Li, *Green Chem.*, 2024, **26**, 9888–9898.

6 T. Fan, J. Zhang, X. Zhang, M. Wang, X. Yi, Y. Lum and Z. Chen, *Nano Energy*, 2024, **130**, 110135.

7 X.-Q. Duan, G.-Y. Duan, Y.-F. Wang, X.-Q. Li, R. Wang, R. Zhang and B.-H. Xu, *Small*, 2023, **19**, 2207219.

8 T. Wang, J. Chen, X. Ren, J. Zhang, J. Ding, Y. Liu, K. H. Lim, J. Wang, X. Li, H. Yang, Y. Huang, S. Kawi and B. Liu, *Angewandte Chemie International Edition*, 2023, **62**, e202211174.

9 R. Samanta, M. Kempasiddaiah, R. K. Trivedi, B. Chakraborty and S. Barman, *ACS Appl. Energy Mater.*, 2024, **7**, 5359–5370.

10 B. Li, J. Chen, L. Wang, D. Xia, S. Mao, L. Xi, S. Ying, H. Zhang and Y. Wang, *Applied Catalysis B: Environment and Energy*, 2025, **363**, 124784.

11 Z. Liu, C. Liu, S. Mao and X. Huang, *ACS Appl. Mater. Interfaces*, 2023, **15**, 7529–7537.

12 Y. Fu, B. Zeng, X. Wang, L. Lai, Q. Wu and K. Leng, *Chemistry – A European Journal*, 2024, **30**, e202402301.

13 W. Cheng, X. Xu, Q. Liao, G. Yao, C. Zhang and H. Li, *Chemical Engineering Journal*, 2024, **480**, 147922.

14 Y. Shi, Y. Wang, J. Yu, Y. Chen, C. Fang, D. Jiang, Q. Zhang, L. Gu, X. Yu, X. Li, H. Liu and W. Zhou, *Advanced Energy Materials*, 2023, **13**, 2203506.

15 R. Francke, B. Schille and M. Roemelt, *Chem. Rev.*, 2018, **118**, 4631–4701.

16 N. Han, P. Ding, L. He, Y. Li and Y. Li, *Advanced Energy Materials*, 2020, **10**, 1902338.

17 C. Costentin, S. Drouet, G. Passard, M. Robert and J.-M. Savéant, *J. Am. Chem. Soc.*, 2013, **135**, 9023–9031.

18 J. Gu, F. Héroguel, J. Luterbacher and X. Hu, *Angewandte Chemie International Edition*, 2018, **57**, 2943–2947.

19 Z.-Z. Niu, L.-P. Chi, R. Liu, Z. Chen and M.-R. Gao, *Energy Environ. Sci.*, 2021, **14**, 4169–4176.

20 N. Dutta, D. Bagchi, G. Chawla and S. C. Peter, *ACS Energy Lett.*, 2024, **9**, 323–328.